Geochemical Perspectives Letters

Fast REE re-distribution in mantle clinopyroxene *via* reactive melt infiltration

G. Borghini[1*], P. Fumagalli[1], F. Arrigoni[1], E. Rampone[2], J. Berndt[3], S. Klemme[3], M. Tiepolo[1]

https://doi.org/10.7185/geochemlet.2323

Abstract

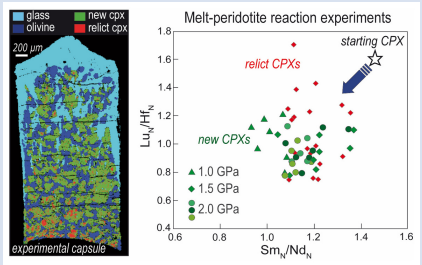

Melt-mineral interactions may strongly affect the mineralogy and chemistry of the upper mantle. Although the grain-scale processes governing the interaction have been theoretically investigated, the efficiency of melt-rock reaction in re-distributing trace elements in mantle clinopyroxene still remains to be experimentally evaluated. We performed high pressure reaction experiments at 1–2 GPa, 1200–1350 °C, on homogeneous mixtures of LREE-depleted clinopyroxene, San Carlos olivine and an Enriched-MORB glass. Melt-peridotite reaction leads to textural replacement of mantle clinopyroxene by dissolution and precipitation as a function of temperature and run duration. Experimental results indicate that rapid modification of the REE signature of mantle clinopyroxene occurs not only *via* dissolution and precipitation but even *via* trace element diffusion within unreacted crystal relicts. The extent of reacted melt crystallisation influences the REE fractionation in modified clinopyroxene. Aided by a high reaction rate, local chemical equilibrium between clinopyroxene and melt can be approached even at the time scale of the experiments. Results from this study demonstrate that infiltration of REE-enriched melt within a mantle peridotite is capable of completely resetting the pristine trace element budget of mantle clinopyroxene.

Received 12 December 2022 | Accepted 20 June 2023 | Published 25 July 2023

Introduction

Porous flow is the main mechanism of melt transport in the deep hot mantle and within the thermal boundary layer. Reaction between mantle minerals and transient melts may strongly affect the mineralogy and chemistry of the upper mantle (*e.g.*, Rampone *et al.*, 2020, and references therein). Modal and chemical changes in mantle peridotite can occur as a result of diffuse porous flow, or by focused melt infiltration related to melt-bearing conduits (dunite channels), or pyroxenitic veins and layers (mantle re-fertilization; *e.g.*, Warren, 2016). Melt-rock reactions are therefore able to modify large portions of the mantle and create chemical and isotopic heterogeneity at different length scales and geological settings.

Changes in mineral abundances and chemistry are mainly controlled by physical parameters, as well as the composition and amount (*i.e.* the melt-rock ratio) of the reacting melt. The interaction between an infiltrating melt and partially molten peridotite is controlled by grain-scale processes that involve dissolution, precipitation, reprecipitation and diffusive exchange between the interstitial melt and surrounding crystals (Liang, 2003). Several numerical and theoretical studies investigated the role and kinetics of these grain-scale processes (*e.g.*, Navon and Stolper, 1987; Hauri, 1997; Van Orman *et al.*, 2002) and laboratory experiments successfully reproduced textural and chemical variations observed in natural mantle samples (*e.g.*, Morgan and Liang, 2005; Van den Bleeken *et al.*, 2010; Wang *et al.*, 2020). However, very few experimental studies have directly investigated the trace element (re-)distribution in mantle minerals resulting from melt-peridotite reaction (Lo Cascio *et al.*, 2008; Yao *et al.*, 2012; Ma and Shaw, 2021) which is mostly due to analytical difficulties in measuring trace element concentrations of fine-grained experimental phases. In particular, the efficiency of melt-rock reaction in modifying or resetting the trace element composition of mantle clinopyroxene, which is the main trace element carrier in spinel peridotites (about 1–2 GPa), still remains to be experimentally evaluated.

We performed high pressure reaction experiments at 1–2 GPa, 1200–1350 °C, on homogeneous mixtures of clinopyroxene (250–160 µm), olivine and an enriched MORB melt (Table S-1 and Fig. S-1; full description of experimental details in Supplementary Information). Initial weight proportions among basalt, clinopyroxene and olivine are 1:1:1, except for one run performed with a mix of 2:1:1, respectively (Table S-2). Such a high melt/rock ratio is consistent with previous melt transport experiments (*e.g.*, Lambart *et al.*, 2009) or melt-peridotite interaction occurring in the host mantle of pyroxenite veins (Bodinier *et al.*, 2004). Adopting a simplified mantle assemblage (olivine + clinopyroxene) promoted the development of coarse textures suitable for the analysis of the trace element composition with laser

1. Dip. Scienze Terra, University of Milano, 20133 Milano, Italy
2. DISTAV, University of Genova, 16132 Genova, Italy
3. Institut fuer Mineralogie, Westfalische Wilhelms Universitat Muenster, Muenster, Germany
* Corresponding author (email: giulio.borghini@unimi.it)

ablation ICP-MS techniques. Here we experimentally determine textural and chemical effects of reactive infiltration/migration of REE-enriched melt within a mantle peridotite with particular focus on REE re-distribution *via* melt-clinopyroxene interaction at asthenosphere-lithosphere conditions.

Melt-Peridotite Reaction Experiments

All experiments produced chemical and textural evidence of the reaction $melt_1 + cpx_1 + ol_1 = melt_2 + cpx_2 + ol_2$, implying the dissolution and recrystallisation of olivine and clinopyroxene (Table S-2). Accordingly, at 1–2 GPa clinopyroxene is the liquidus phase for the selected basaltic glass (Fig. S-2). In the long duration runs (≥48 h), olivine has rather homogeneous major element compositions marked by higher CaO and lower NiO and X_{Mg} [$X_{Mg} = Mg/(Mg + Fe^{tot})$] than the initial SC olivine (Fig. S-3), as observed in basalt-dunite reaction experiments (Borghini *et al.*, 2018). New crystallised clinopyroxene has partially replaced the starting clinopyroxene forming rims on initial clinopyroxene relics or homogeneous grains precipitated by the reacted melt (Fig. 1a, c). New clinopyroxenes have lower Ca and Cr contents and higher Na concentrations with respect to the initial clinopyroxene (Fig. S-2, Tables S-3 and S-4). By contrast, most clinopyroxene relics preserve the initial major element composition (Fig. 1, Tables S-3 and S-4). Al_{IV} content in clinopyroxene varies within a rather narrow range in a single experiment and tends to be higher in the runs with a high degree of crystallisation or a higher initial melt proportion (Fig. S-3). Reacted glasses still retain basaltic major element compositions but exhibit higher X_{Mg} than the initial basalt (Table S-6) due to reaction with mantle phases.

Image analysis, derived by combining X-ray concentration maps, provided estimates of modal variations caused by the reaction (Figs. 1b, S-2 and Table S-2). The degree of clinopyroxene textural replacement (new cpx/relict cpx ratio) increases with temperature and run duration (Fig. 1d). At 1.5 GPa, 1300 °C, and 2 GPa, 1350 °C, clinopyroxene is almost completely renewed by reaction with the melt, in runs of 69 and 48 hours, respectively. The extent of reacted melt crystallisation in experiments increases with increasing pressure and/or decreasing temperature, as demonstrated by the low final melt/rock ratio in experiment at 2 GPa and 1300 °C (Table S1 and Fig. S-2).

REE Distribution after Melt-Cpx Interaction

Consistent with the fast diffusion in silicate melt, experimental glasses have homogeneous trace element concentrations, and show LREE-HREE fractionation ($La_N/Yb_N = 1.74–3.66$) slightly lower than the initial glass ($La_N/Yb_N = 5.49$), mostly reflecting the dissolution of LREE-depleted clinopyroxene (Table S-9). Compared to the starting clinopyroxene, the new clinopyroxenes

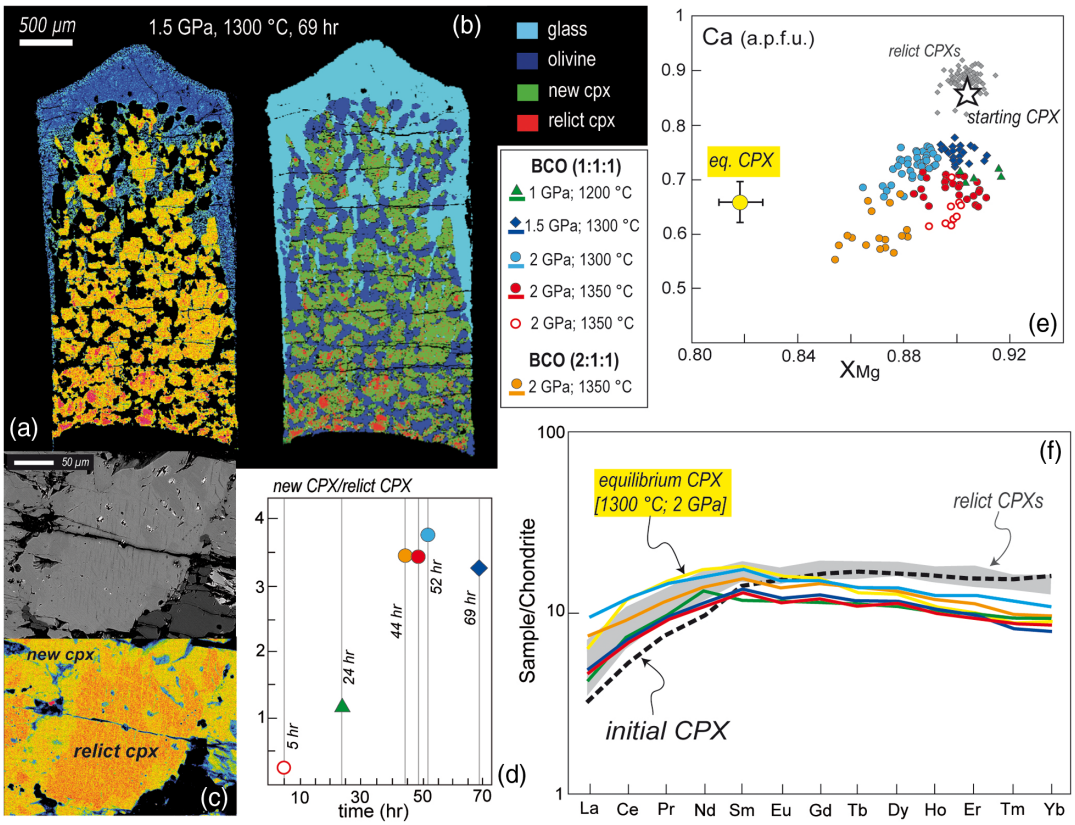

Figure 1 **(a)** Map of Ca distribution in the whole capsule after reaction experiments on Basalt:Clinopyroxene:Olivine (BCO) 1:1:1, at 1.5 GPa and 1300 °C; red areas (high Ca) depict relicts of starting clinopyroxene. **(b)** Phase map derived by combining X-ray concentration maps (Ca, Mg, Al). **(c)** Backscattered electron (BSE) image and Ca map showing details of Ca-rich relict clinopyroxene that is partially substituted by rims of new crystallised clinopyroxene. **(d)** New cpx/relict cpx ratio (*i.e.* clinopyroxene textural replacement) *versus* run duration of experiments (time, hours). **(e)** Ca (a.p.f.u.) *versus* X_{Mg} value [$Mg/(Mg + Fe_{tot})$] of starting, new and relict clinopyroxenes in reaction experiments; also shown is the composition of clynopyroxene in equilibrium crystallisation experiments at 2 GPa and 1300 °C. **(f)** Chondrite normalized REE patterns of average clinopyroxene in reaction and crystallisation experiments compared to the average REE pattern of starting clinopyroxene; grey field is defined by REE patterns of relict clinopyroxenes.

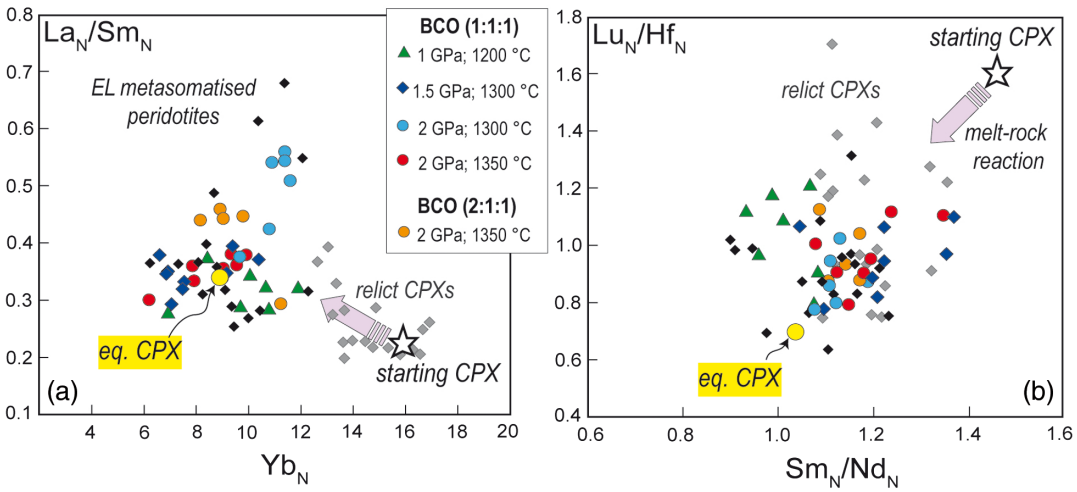

Figure 2 Chondrite normalised **(a)** La_N/Sm_N *versus* Yb_N and **(b)** Sm_N/Nd_N *versus* Lu_N/Hf_N of initial, new and relict clinopyroxene from reacted and crystallisation experiments compared to data of clinopyroxenes in metasomatised peridotites from Northern Apennine veined mantle (black diamonds, Borghini *et al.*, 2020).

show REE patterns characterised by a systematic lowering of HREE and MREE and increasing fractionation of LREE over the MREE reflecting the crystallisation from enriched reacted melts (Fig. 1f). Remarkably, relict clinopyroxenes are modified; the slight but systematic LREE (and Sm) enrichment compared to the starting clinopyroxene (Fig. 1f) reflects partial REE re-equilibration *via* diffusion presumably driven by the more pronounced difference in LREE concentration between initial clinopyroxene and melt, at rather close HREE abundances. REE diffusion within cpx relics coincides with dissolution and precipitation during the interaction with melts (Lo Cascio *et al.*, 2008). Theoretical studies revealed that REE fractionation *via* diffusion is rather sluggish during melt porous flow (*e.g.*, Van Orman *et al.*, 2002; Liang, 2003). However, REE diffusion over a distance of less than 200 μm has been observed in reaction couple experiments (Lo Cascio *et al.*, 2008). In our experimental setup both dissolution and reprecipitation and solid-liquid REE diffusion into the relict clinopyroxenes occur, thus resulting in the whole chemical modification of the initial mantle clinopyroxene at sizes lower than 250 μm, along 2–3 day experiments. These results indicate that rapid textural replacement of relict clinopyroxene strongly improves trace element remobilisation, even for LREE having low diffusion rate (Van Orman *et al.*, 2001).

New clinopyroxenes show clockwise-rotated average REE patterns (Fig. 1f), very similar to REE patterns computed in studies that documented the effect of interaction between enriched melts and residual clinopyroxene within pyroxenite-bearing veined peridotite (Borghini *et al.*, 2020), or during melt infiltration during open system mantle melting, to explain the trace element variability of abyssal peridotite (Brunelli *et al.*, 2014). We found that the fractionation of LREE over the MREE varies as a function of experimental conditions. In particular, clinopyroxenes in experiments that experienced the highest extent of reacted melt crystallisation at 2 GPa and 1300 °C (Fig. 2a) exhibit high La_N/Sm_N ratios ($La_N/Sm_N = 0.42–0.56$), reflecting REE fractionation of crystallising reacted melt. Moreover, high La_N/Sm_N ratios in new clinopyroxenes have been found in the reaction experiment with a higher amount of starting basalt. Similar high La_N/Sm_N ratios have been documented in mantle peridotites inferred to be metasomatised by E-MORB-like melts coming from pyroxenitic veins (Northern Apennine veined mantle; Borghini *et al.*, 2020). Ancient events of melt infiltration in those peridotites modified the trace element composition of clinopyroxene by lowering Sm_N/Nd_N and Lu_N/Hf_N ratios that, over time, formed mantle domains with enriched Nd-Hf isotopic signatures (Borghini *et al.*, 2021). Our experimental results show that high pressure and temperature interaction with E-MORB-type basalt causes rapid decrease of Sm_N/Nd_N and Lu_N/Hf_N ratios in newly formed clinopyroxene relative to the starting

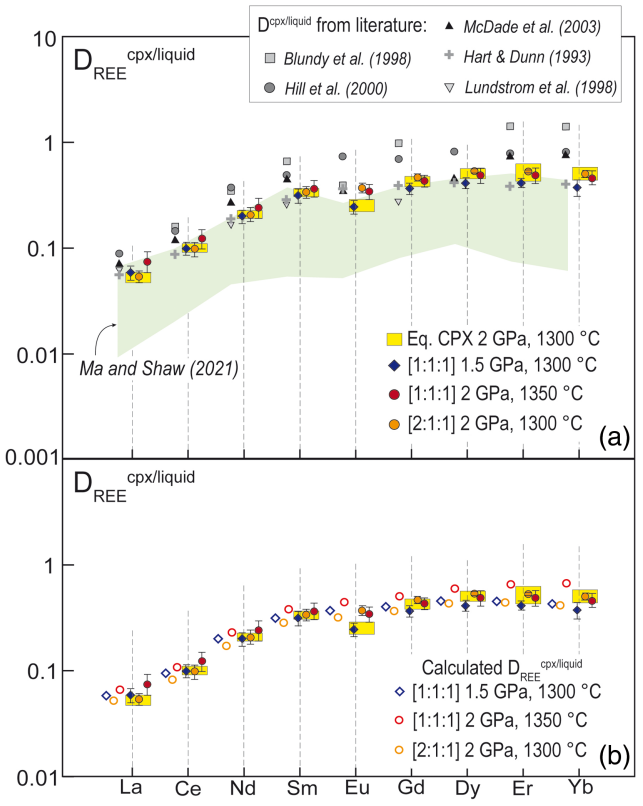

Figure 3 "Reaction" $D_{REE}^{cpx/liquid}$ from this study compared to **(a)** $D_{REE}^{cpx/liquid}$ derived by equilibrium crystallisation experiment at 2 GPa and 1300 °C and those from the literature (list of references is in the text), and **(b)** the $D_{REE}^{cpx/liquid}$ provided by the application of the parameterised lattice strain model by Sun and Liang (2012), to each reaction experiments of this study.

composition (Fig. 2b). In addition, diffusion combined with dissolution and reprecipitation results in variable but systematic chemical changes in clinopyroxene relics, again towards lower Sm_N/Nd_N and Lu_N/Hf_N ratios (Fig. 2b).

Using the REE concentrations measured in new clinopyroxenes and texturally associated glasses, we computed "reaction" cpx/melt distribution coefficients (Fig. 3a), which are comparable to those derived by equilibrium experiments (Hart and Dunn, 1993; Blundy *et al.*, 1998; Lundstrom *et al.*, 1998; Hill *et al.*, 2000; McDade *et al.*, 2003). These also closely overlap the equilibrium distribution coefficients measured for REE in our crystallisation run at 2 GPa and 1300 °C and those computed using parameterisation by Sun and Liang (2012) based on the composition of clinopyroxenes in our reaction experiments (Fig. 3b). This suggests that new clinopyroxenes and reacted melt approached the chemical equilibrium even at the time scale of the experiment. These experiments reveal that small (<250 μm) mantle clinopyroxene is rapidly modified by a single step of interaction with a REE-enriched transient melt. In a scenario of multiple melt injections, porous migration of melts enriched in trace elements may efficiently refertilise mantle clinopyroxene (*e.g.*, Brunelli *et al.*, 2014). Several interactions with REE-depleted clinopyroxene are expected to progressively smooth the LREE-HREE fractionation of a single batch of transient melt, as found in reacted glasses of this study, confirming the important role of melt transport processes in the chemical variations of erupted basalts (Navon and Stolper, 1987).

Conclusions

New experimental results demonstrate that melt-peridotite reaction is efficient in modifying the REE signature of mantle clinopyroxene by a combination of dissolution, precipitation and trace element diffusion. High reaction rate leads to local chemical equilibrium between clinopyroxene and melt even at the time scale of the experiments. These data demonstrate that infiltration of REE-enriched melt within a mantle peridotite is potentially able to completely reset the pristine trace element budget of clinopyroxene.

Acknowledgements

We thank two anonymous reviewers for constructive reviews and Anat Shahar for editorial handling. We greatly thank A. Cipriani for providing the starting basaltic glass. A. Risplendente and G. Sessa are thanked for technical assistance during the work at the electron microprobe and LA-ICP-MS, respectively, at University of Milano. Our thanks also go to B. Schmitte at the University of Münster for her excellent support during the LA-ICP-MS analyses that were done in the midst of the international Covid19 pandemic.

Editor: Anat Shahar

Additional Information

Supplementary Information accompanies this letter at https://www.geochemicalperspectivesletters.org/article2323.

Cite this letter as: Borghini, G., Fumagalli, P., Arrigoni, F., Rampone, E., Berndt, J., Klemme, S., Tiepolo, M. (2023) Fast REE re-distribution in mantle clinopyroxene *via* reactive melt infiltration. *Geochem. Persp. Let.* 26, 40–44. https://doi.org/10.7185/geochemlet.2323

References

Blundy, J.D., Robinson, J.A.C., Wood, B.J. (1998) Heavy REE are compatible in clinopyroxene on the spinel lherzolite solidus. *Earth and Planetary Science Letters* 160, 493–504. https://doi.org/10.1016/S0012-821X(98)00106-X

Bodinier, J.-L., Menzies, M.A., Shimizu, N., Frey, F.A., McPherson, E. (2004) Silicate, Hydrous and Carbonate Metasomatism at Lherz, France: Contemporaneous Derivatives of Silicate Melt–Harzburgite Reaction. *Journal of Petrology* 45, 299–320. https://doi.org/10.1093/petrology/egg107

Borghini, G., Francomme, J.E., Fumagalli, P. (2018) Melt-dunite interactions at 0.5 and 0.7 GPa: experimental constraints on the origin of olivine-rich troctolites. *Lithos* 323, 44–57. https://doi.org/10.1016/j.lithos.2018.09.022

Borghini, G., Rampone, E., Zanetti, A., Class, C., Fumagalli, P., Godard, M. (2020) Ligurian pyroxenite-peridotite sequences (Italy) and the role of melt-rock reaction in creating enriched-MORB mantle sources. *Chemical Geology* 532, 119252. https://doi.org/10.1016/j.chemgeo.2019.07.027

Borghini, G., Rampone, E., Class, C., Goldstein, S., Cai, Y., Cipriani, A., Hofmann, A.W., Bolge, L. (2021) Enriched Hf–Nd isotopic signature of veined pyroxenite-infiltrated peridotite as a possible source for E-MORB. *Chemical Geology* 586, 120591. https://doi.org/10.1016/j.chemgeo.2021.120591

Brunelli, D., Paganelli, E., Seyler, M. (2014) Percolation of enriched melts during incremental open-system melting in the spinel field: A REE approach to abyssal peridotites from the Southwest Indian Ridge. *Geochimica et Cosmochimica Acta* 127, 190–203. https://doi.org/10.1016/j.gca.2013.11.040

Hart, S.R., Dunn, T. (1993) Experimental cpx/melt partitioning of 24 trace elements. *Contributions to Mineralogy and Petrology* 113, 1–8. https://doi.org/10.1007/BF00320827

Hauri, E.H. (1997) Melt migration and mantle chromatography, 1: simplified theory and conditions for chemical and isotopic decoupling. *Earth and Planetary Science Letters* 153, 1–19. https://doi.org/10.1016/S0012-821X(97)00157-X

Hill, E., Wood, B.J., Blundy, J.D. (2000) The effect of Ca-Tschermaks component on trace element partitioning between clinopyroxene and silicate melt. *Lithos* 53, 203–215. https://doi.org/10.1016/S0024-4937(00)00025-6

Lambart, S., Laporte, D., Schiano, P. (2009) An experimental study of focused magma transport and basalt–peridotite interactions beneath mid-ocean ridges: implications for the generation of primitive MORB compositions. *Contributions to Mineralogy and Petrology* 157, 429–451. https://doi.org/10.1007/s00410-008-0344-7

Liang, Y. (2003) Kinetics of crystal-melt reaction in partially molten silicates: 1. Grain scale processes. *Geochemistry, Geophysics, Geosystems* 4, 1045. https://doi.org/10.1029/2002GC000375

Lo Cascio, M., Liang, Y., Shimizu, N., Hess, P.C. (2008) An experimental study of the grain-scale processes of peridotite melting: implications for major and trace element distribution during equilibrium and disequilibrium melting. *Contributions to Mineralogy and Petrology* 156, 87–102. https://doi.org/10.1007/s00410-007-0275-8

Lundstrom, C.C., Shaw, H.F., Ryerson, F.J., Williams, Q., Gill, J. (1998) Crystal chemical control of clinopyroxene-melt partitioning in the Di-Ab-An system: implications for elemental fractionations in the depleted mantle. *Geochimimica et Cosmochimica Acta* 62, 2849–2862. https://doi.org/10.1016/S0016-7037(98)00197-5

Ma, S., Shaw, C.S.J. (2021) An Experimental Study of Trace Element Partitioning between Peridotite Minerals and Alkaline Basaltic Melts at 1250°C and 1 GPa: Crystal and Melt Composition Impacts on Partition Coefficients. *Journal of Petrology* 62, egab084. https://doi.org/10.1093/petrology/egab084

McDade, P., Blundy, J.D., Wood, B.J. (2003) Trace element partitioning on the Tinaquillo Lherzolite solidus at 1.5 GPa. *Physics of the Earth and Planetary Interiors* 139, 129–147. https://doi.org/10.1016/S0031-9201(03)00149-3

Morgan, Z., Liang, Y. (2005) An experimental study of the kinetics of lherzolite reactive dissolution with applications to melt channel formation. *Contributions to Mineralogy and Petrology* 150, 369–385. https://doi.org/10.1007/s00410-005-0033-8

Navon, O., Stolper, E. (1987) Geochemical Consequences of Melt Percolation: The Upper Mantle as a Chromatographic Column. *The Journal of Geology* 95, 285–307. https://doi.org/10.1086/629131

Rampone, E., Borghini, G., Basch, V. (2020) Melt migration and melt-rock reaction in the Alpine-Apennine peridotites: Insights on mantle dynamics in extending lithosphere. *Geoscience Frontiers* 11, 151–166. https://doi.org/10.1016/j.gsf.2018.11.001

Sun, C., Liang, Y. (2012) Distribution of REE between clinopyroxene and basaltic melt along a mantle adiabat: effects of major element composition, water, and temperature. *Contributions to Mineralogy and Petrology* 163, 807–823. https://doi.org/10.1007/s00410-011-0700-x

Van Den Bleeken, G., Müntener, O., Ulmer, P. (2010) Reaction Processes between Tholeiitic Melt and Residual Peridotite in the Uppermost Mantle: an Experimental Study at 0.8 GPa. *Journal of Petrology* 51, 153–183. https://doi.org/10.1093/petrology/egp066

Van Orman, J.A., Grove, T.L., Shimizu, N. (2001) Rare earth element diffusion in diopside: influence of temperature, pressure, and ionic radius, and an elastic model for diffusion in silicates. *Contributions to Mineralogy and Petrology* 141, 687–703. https://doi.org/10.1007/s004100100269

Van Orman, J.A., Grove, T.L., Shimizu, N. (2002) Diffusive fractionation of trace elements during production and transport of melt in Earth's upper mantle. *Earth and Planetary Science Letters* 198, 93–112. https://doi.org/10.1016/S0012-821X(02)00492-2

Wang, C., Lo Cascio, M., Liang, Y., Xu, W. (2020) An experimental study of peridotite dissolution in eclogite-derived melts: Implications for styles of melt-rock interaction in lithospheric mantle beneath the North China Craton. *Geochimica et Cosmochimica Acta* 278, 157–176. https://doi.org/10.1016/j.gca.2019.09.022

Warren, J.M. (2016) Global variations in abyssal peridotite compositions. *Lithos* 248–251, 193–219. http://dx.doi.org/10.1016/j.lithos.2015.12.023

Yao, L., Sun, C., Liang, Y. (2012) A parameterized model for REE distribution between low-Ca pyroxene and basaltic melts with applications to REE partitioning in low-Ca pyroxene along a mantle adiabat and during pyroxenite-derived melt and peridotite interaction. *Contributions to Mineralogy and Petrology* 164, 261–280. https://doi.org/10.1007/s00410-012-0737-5

Geochemical Perspectives Letters

Fast REE re-distribution in mantle clinopyroxene *via* reactive melt infiltration

G. Borghini, P. Fumagalli, F. Arrigoni, E. Rampone, J. Berndt, S. Klemme, M. Tiepolo

Supplementary Information

The Supplementary Information includes:

- Experimental Procedure
- Analytical Techniques
- Tables S-1 to S-10
- Figures S-1 to S-3
- Supplementary Information References

Experimental Procedure

Experiments were performed at 1, 1.5 and 2 GPa on homogeneous mixtures of glass and minerals. Selected tholeiitic basaltic glass from Romanche Fracture Zone is moderately evolved (X_{Mg} = 0.60, $Na_2O + K_2O$ = 4.29 wt. % and displays Enriched-MORB (E-MORB)-like trace element signatures (La_N/Sm_N = 1.90, Sm_N/Yb_N = 2.71; data normalised to chondrite; Anders and Grevesse, 1989; Fig. S-1, Table S-1). We used a simplified mantle assemblage made by olivine and clinopyroxene in order to enhance the growth of clinopyroxene rims large enough to be analysed by laser ablation ICP-MS techniques.

The mantle peridotite component is simulated by mixing in equal proportions San Carlos olivine (Fo_{90}) and clinopyroxene separated from a fertile lherzolite from Northern Apennine ophiolitic sequences (BG6 sample, Borghini *et al.*, 2011). The clinopyroxene grains consist of spinel-facies porphyroclasts that contain very thin (2–10 μm) orthopyroxene exsolutions. Average clinopyroxene composition is X_{Mg} of 0.90 with moderate Al, high Ca and low Na (Al_2O_3 = 7.53 wt. %, CaO = 21.87 wt. %, Na_2O = 0.81 wt. %; Table S-1). The trace element composition is characterised by a slightly depleted LREE pattern (La_N/Sm_N = 0.23) and nearly flat MREE-HREE patterns at about 10× CI (Fig. S-1), which is typical of clinopyroxenes in equilibrium with Normal (N-) MORB (*e.g.*, Hofmann, 1988; Gale *et al.*, 2013). San Carlos olivine and BG6 clinopyroxene crystals were crushed in a boron carbide mortar and then sieved, selecting the olivine grains <63 μm and clinopyroxene crystals between 160 and 250 μm in size. We used a larger grain size of initial clinopyroxene to evaluate the rate of clinopyroxene textural replacement by the reaction with the melt as a function of experimental temperature and run duration. The basaltic glass was leached to remove potential sea-water-related contamination: glass chips were crushed, then placed in a beaker, covered by 8 N HNO_3 and then placed in a ultrasonic bath for 10 minutes. The leached glass was dried in oven at 60 °C for a minimum of two hours and crushed in ethanol in an agate mortar. The weighting procedure of starting materials mixing was carried out with a precision balance to five decimal places. We prepared two starting material mixtures with proportions of 1:1:1 and 2:1:1 of basalt:clinopyroxene:olivine, respectively, in order to investigate the effect of two initial

melt/peridotite ratios. Experiments were carried out using the "rocking" end-loaded piston cylinder at the Laboratorio di Petrologia Sperimentale, Dipartimento di Scienze della Terra "A. Desio", University of Milan, using talc-pyrex-MgO piston cylinder assemblies. A pressure correction for friction of 10 % was experimentally calibrated using the quartz-coesite transition (Bohlen and Boettcher, 1982). A graphite inner capsule granted the chemical isolation of the sample from the outer Pt-capsule thus minimising the Fe loss, and it also maintained the oxygen fugacity of the experiments below the graphite–CO buffer (*e.g.*, Ulmer and Luth, 1991; Medard *et al.*, 2008). To ensure nominally anhydrous conditions, the graphite lined Pt-capsule with the starting material was dried in oven at 250 °C for a minimum of three hours, before it was welded shut. Temperatures were measured with type S thermocouples (with an accuracy of ±5 °C) that were separated from the Pt capsule by a 0.6-mm thick hard alumina disc. According to piston cylinder calibration, pressure uncertainties are within ±3 %. We terminated the runs by turning off the electrical power, which resulted in initial quench rates of about 90 °C/sec. Capsules were cleaned with an abrasive tip, enclosed in epoxy, sectioned lengthwise and polished with diamond paste.

Analytical Techniques

Major elements microanalyses were performed using a JEOL JXA 8200 Superprobe at the Dipartimento di Scienze della Terra "Ardito Desio", University of Milan. Analyses on experimental minerals were acquired using 1 µm beam size, with an acceleration voltage of 15 kV and a beam current of 15 nA. Typical acquisition time was 30 s counting on peaks and 10 s counting on the background. In order to prevent alkali loss, we analysed glass using a beam size of 5 µm.

X-ray maps allowed image analysis using the *Fiji Image* processing package of *ImageJ software* (Rueden *et al*., 2017), which provided reliable estimates of modal abundances after the reaction experiments. Trace elements of the experimental run products were measured in two independent laboratories. Trace element concentrations in the experiment run products were determined by laser ablation inductively coupled plasma mass spectrometry (LA-ICP-MS) analyses at the Institute for Mineralogy, Universität Münster. Ablation of target materials was performed using a pulsed 193 nm ArF excimer laser (Analyte G2, Photon Machines), with a repetition rate of 10 Hz and an energy of ~3–4 J/cm^2. Depending on the dimensions of the target material, beam diameters were varied between 10 and 65 µm. The following isotopes were measured: ^{7}Li, ^{11}B, ^{29}Si, ^{43}Ca, ^{49}Ti, ^{51}V, ^{53}Cr, ^{55}Mn, 59Co, ^{60}Ni, ^{63}Cu, ^{66}Zn, ^{69}Ga, ^{73}Ge, ^{85}Rb, ^{88}Sr, ^{89}Y, ^{90}Zr, ^{93}Nb, ^{95}Mo, ^{133}Cs, ^{137}Ba, ^{139}La, ^{140}Ce, ^{141}Pr, ^{146}Nd, ^{147}Sm, ^{153}Eu, ^{157}Gd, ^{159}Tb, ^{163}Dy, ^{165}Ho, ^{166}Er, ^{169}Tm, ^{172}Yb, ^{175}Lu, ^{178}Hf, ^{181}Ta, ^{182}W, ^{208}Pb, ^{232}Th and ^{238}U. The analyses were calibrated using the NIST 610 glass reference material as a primary standard, with standard measurements acquired after approximately every 20 samples analyses. Additional measurements were made of the NIST 612 glass, as well as the USGS BIR-1G and BHVO-2G glass reference materials. Internal standards for the analyses were Si and Ca, obtained from the EMPA dataset and (in the case of the reference materials) the GeoReM database (Jochum *et al.*, 2011). Averages of all the NIST 610 glass measurements were within 2 % of the GeoReM values for all elements. Percent relative standard deviation (% r.s.d.) values for the NIST 610 glass measurements were less than 5 % for most elements and typically less than 2 % for the larger, 40–65 µm spots. The % r.s.d. values for repeat measurements of the NIST 612, BIR-1G and BHVO-2G glasses are typically 10–25 % (Table S-10a), and lower than 10 % on average for the 40–65 µm spot diameters. The data were reduced using the GEMOC GLITTER software (Griffin *et al.*, 2008), including monitoring the signal selection to identify and exclude any instances where the beam may have hit inclusions or grain boundaries.

Trace elements concentrations in minerals and glasses were determined with LA-ICP-MS at the Geochemistry, Geochronology and Isotope Geology laboratory of Dipartimento di Scienze della Terra "Ardito Desio", University of Milan. The instrument couples an ArF 193 nm excimer laser microprobe, equipped with HelEx II volume sample chamber (Analyte Excite - Teledyne CETAC), with a quadrupole ICP-MS system (iCAP-RQ Thermo Scientific). Laser spot diameter ranges from 25 to 40 µm as a function of the mineral/glass dimensions. The laser fluence was 2.5 J/cm^2 for glass and clinopyroxene. The laser repetition rate was set to 10 Hz for all minerals. The He flow rate was set to 0.5 L/min and to 0.2 L/min into the sample chamber and in the HelEx II cup, respectively. NIST-612 was used as an external standard, whereas ^{43}Ca and ^{29}Si were adopted as internal standards, depending on the analysed material. Each analysis consisted in the acquisition of a total of 120 s that included 40 s of background signal (comprising 10 s

of laser warm up), about 60 s of laser signal followed by 20 s of wash out time. Quality control was achieved analysing in each analytical run the USGS reference basalt glasses BCR- 2G as unknown. Precision is better than 10 % and accuracy is within 2σ of the preferred values (Table S-10b). Data reduction was carried out using the Glitter software package (Griffin *et al.*, 2008).

EBS images coupled to X-ray maps oriented us in the localisation of ideal microstructural sites where performing laser ablation analyses and this was applied in particular for the analyses on the reaction rims of clinopyroxene. However, despite of development of rather coarse texture in experimental sample, some clinopyroxene analyses likely suffered from the contamination by interstitial glass that resulted in artificial very intense LREE enrichment. In order to avoid such contamination, we filtered trace element data based on the Ba content, *i.e.* selecting analyses with Ba > 1 ppm in agreement with the very low distribution coefficient of Ba between clinopyroxene and silicate melts (*e.g.*, Hart and Dunn, 1993; Ma and Shaw, 2021).

Supplementary Tables

Table S-1 Major (wt. %) and trace (ppm) element compositions of starting materials.

Table S-2 Experimental conditions and run products.

Table S-3 Major element compositions (wt. %) of olivines in reaction experiments.

Table S-4 Major element compositions (wt. %) of new clinopyroxenes in reaction experiments.

Table S-5 Major element compositions (wt. %) of relict clinopyroxenes in reaction experiments.

Table S-6 Major element compositions (wt. %) of reacted glasses in reaction experiments.

Table S-7 Major element compositions (wt. %) of glass and clinopyroxene in crystallisation experiments at 2 GPa and 1300 °C.

Table S-8 Trace element concentrations (ppm) in clinopyroxenes.

Table S-9 Trace element concentrations (ppm) in glasses.

Table S-10 Trace element compositions of standards measured during LA-ICP-MS analyses.

Tables S-1 to S-10 (.xlsx) are available for download from the online version of this article at https://doi.org/10.7185/geochemlet.2323.

Supplementary Figures

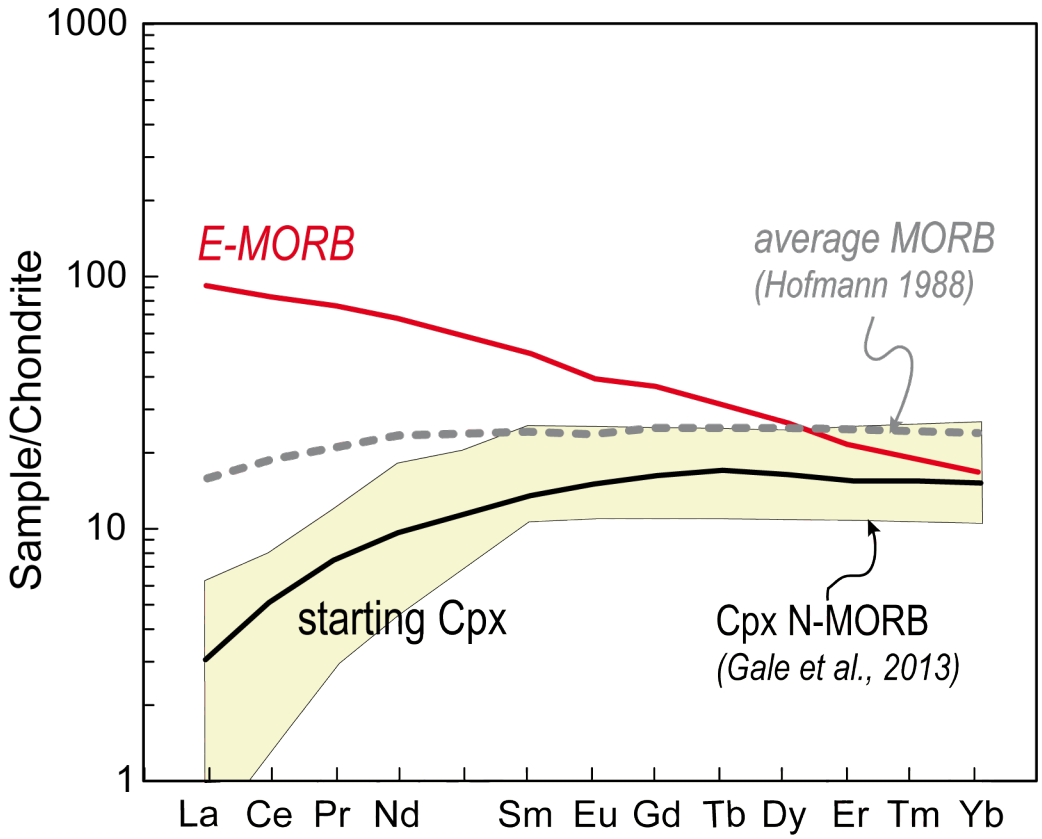

Figure S-1 Chondrite normalised REE patterns of initial clinopyroxene and E-MORB glass used in reaction experiments (from Table S-1). Also reported are the average REE composition of MORB (Hofmann, 1988) and the field defined by computed REE patterns of clinopyroxenes in equilibrium with N-MORB from Gale *et al.* (2013).

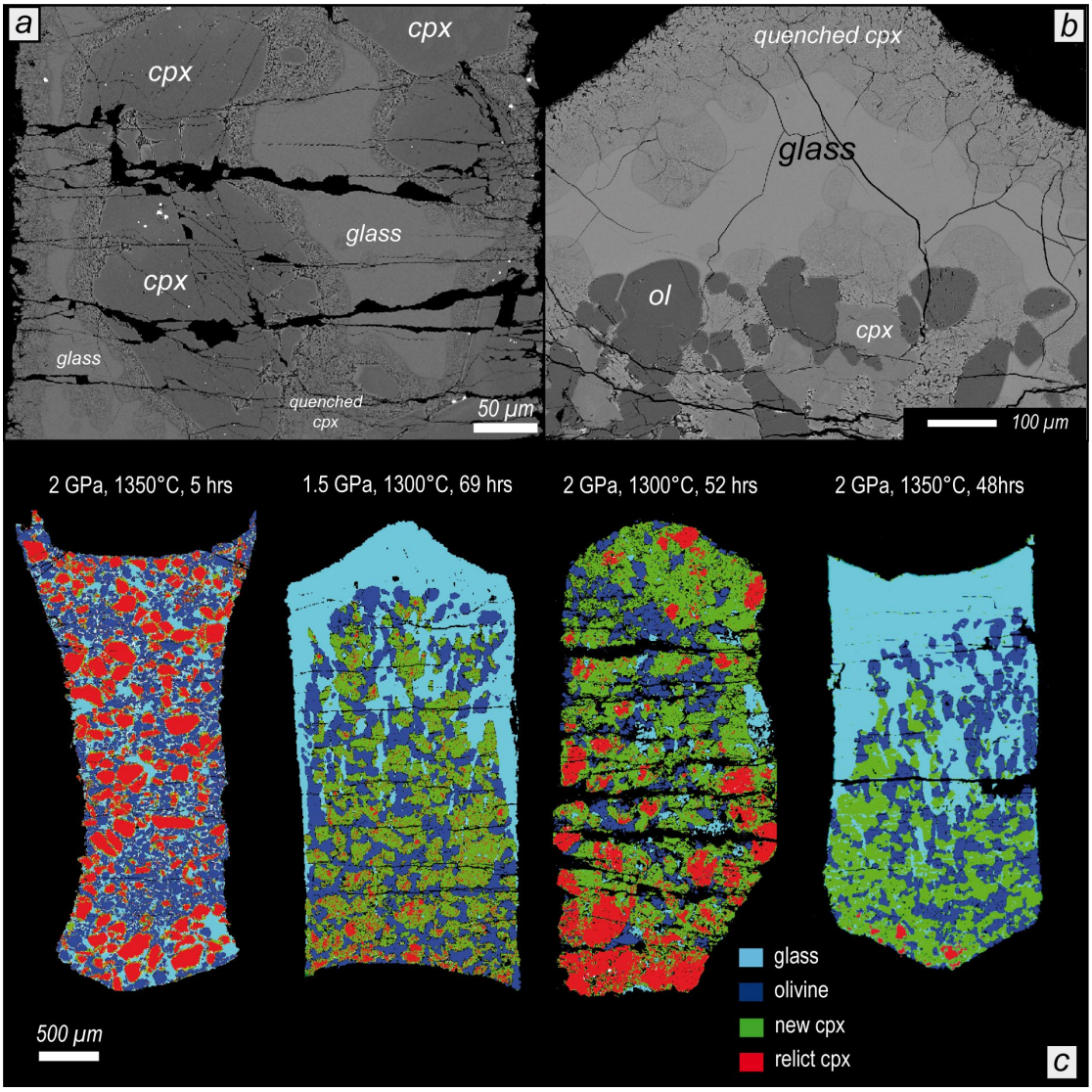

Figure S-2 **(a)** Backscattered electron (BSE) image showing large clinopyroxene grains coexisting with glass in crystallisation experiments at 2 GPa, 1300 °C; the growth of chemically homogeneous, unzoned clinopyroxene grains and mass balance calculation with very low sum of the squares of the residuals (R^2 = 0.1123; 0.19 cpx and 0.81 glass), strongly support the attainemnt of equilibrium in this crystallisation run. **(b)** Run products of reaction experiment at 1.5 GPa and 1300 °C, consisting of rounded olivine, prismatic clinopyroxene and glass. Olivine has straight boundary against glass and clinopyroxene suggesting it requilibrated with reacted glass and new clinopyroxe. No unreacted olivine is identifiable because it always it has homogeneous composition, significantly different from starting SC olivine, as observed in dunite-basalt reaction experiments (Borghini *et al.*, 2018, 2022). Accumulation of reacted glass at the top of experimental charge favored the in situ measurements of trace element concentrations. **(c)** Phase maps derived by combining X-ray concentration maps (Ca, Mg, Al) of reaction experiments at 1.5 and 2 GPa on starting material with basalt:clinopyroxene:olivine weight proportions of 1:1:1. Image analyses revealed that experiment at 2 GPa and 1300 °C experienced high extent of reacted glass crystallisation.

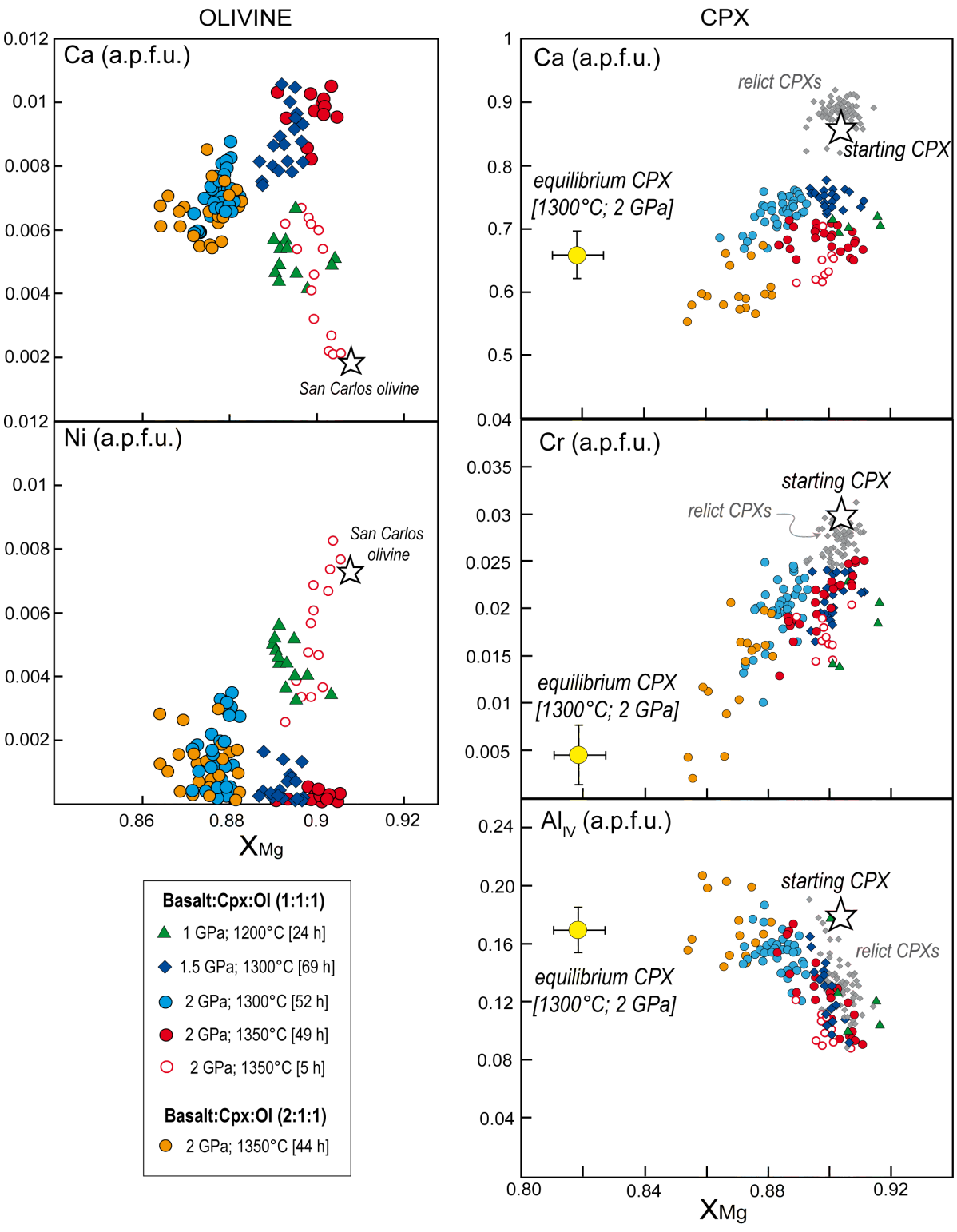

Figure S-3 Major element compositions of olivine (X_{Mg} *versus* Ca and Ni a.p.f.u.) and clinopyroxene (X_{Mg} *versus* Ca, Na and Al_{IV} a.p.f.u.) from crystallisation and reaction experiments. Composition of starting olivine and clinopyroxene are reported for comparison.

Supplementary Information References

Anders, E., Grevesse, N. (1989) Abundances of the elements: meteoric and solar: *Geochimica et Cosmochimica Acta* 53, 197–214. https://doi.org/10.1016/0016-7037(89)90286-X

Bohlen, S.R., Boettcher, A.L. (1982) The quartz -coesite transformation: a precise determination and the effects of other components. *Journal of Geophysical Research* 87, 7073–7078. https://doi.org/10.1029/JB087iB08p07073

Borghini, G., Fumagalli, P., Rampone, E. (2011) The geobarometric significance of plagioclase in mantle peridotites: A link between nature and experiments. *Lithos* 126, 42–53. https://doi.org/10.1016/j.lithos.2011.05.012

Borghini, G., Rampone, E., Zanetti, A., Class, C., Cipriani, A., Hofmann, A. W., Goldstein, S. L. (2016) Pyroxenite layersin the Northern Apennines upper mantle (Italy) – Generation by pyroxenite melting and melt infiltration. *Journal of Petrology* 57, 625–653. https://doi.org/10.1093/petrology/egv074

Borghini, G., Fumagalli P., Francomme J.E. (2018) Melt-dunite interactions at 0.5 and 0.7 GPa: experimental constraints on the origin of olivine-rich troctolites. *Lithos* 323, 44–57. https://doi.org/10.1016/j.lithos.2018.09.022

Borghini, G., Fumagalli, P., Rampone, E. (2022) Melt-rock interactions in a veined mantle: pyroxenite-peridotite reaction experiments at 2 GPa. *European Journal of Mineralogy* 34, 109–129. https://doi.org/10.5194/ejm-34-109-2022

Gale, A., Dalton, C.A., Langmuir, C.H., Su, Y., Schilling, J.G. (2013) The mean composition of ocean ridge basalts. *Geochemistry Geophysics Geosystems* 14, 489–518. https://doi.org/10.1029/2012GC004334

Griffin, W.L., Powell, W., Pearson, N.J., O'Reilly, S.Y. (2008) GLITTER: data reduction software for laser ablation ICP-MS. In Sylvester, P. (ed.), Laser Ablation ICP-MS in the Earth Sciences: Current practices and outstanding issues: Mineralogical Association of Canada, Short Course Series, 40, p. 307-311.

Hart, S.R., Dunn, T. (1993) Experimental cpx/melt partitioning of twenty-four trace elements. *Contributions to Mineralogy and Petrology* 113, 1–8. https://doi.org/10.1007/BF00320827

Hofmann, A.W. (1988) Chemical differentiation of the earth: the relationships between mantle, continental crust and oceanic crust. *Earth and Planetary Science Letters* 90, 297–314. http://dx.doi.org/10.1016/0012-821X(88)90132-X

Jochum, K.P., Wang, X., Nohl, U., Schmidt, S., Schwager, B., Stoll, B., Yang, Q., Weis, U. (2011) Geostandards and geoanalytical research bibliographic review 2010. *Geostandards and Geoanalytical Research* 35, 485–488. https://doi.org/10.1111/j.1751-908X.2011.00164.x

Ma, S., Shaw, C.S.J. (2021) An experimental study of trace element partitioning between peridotite minerals and alkaline basaltic melts at 1250°C and 1 GPa: crystal and melt composition impacts on partition coefficients. *Journal of Petrology* 62, 1–27. https://doi.org/10.1093/petrology/egab084

Médard, E., McCammon, C.A., Barr, J.A., Grove, T.L. (2008) Oxygen fugacity, temperature reproducibility, and H_2O contents of nominally anhydrous piston-cylinder experiments using graphite capsules. *American Mineralogist* 93, 1838–1844. https://doi.org/10.2138/am.2008.2842

Rueden, C.T., Schindelin, J., Hiner, M.C., DeZonia, B.E., Walter, A.E., Arena, E.T., Eliceiri, K.W. (2017) ImageJ2: ImageJ for the next generation of scientific image data. *BMC Bioinformatics*, 18, 529. https://doi.org/10.1186/s12859-017-1934-z

Ulmer, P., Luth, R.W. (1991) The graphite fluid equilibrium in P, T, fO_2 space: an experimental determination to 30 kbar and 1600°C. *Contributions to Mineralogy and Petrology* 106, 265–272. https://doi.org/10.1007/BF00324556